Available online at www.sciencedirect.com
SCIENCE DIRECT®
Polymer 44 (2003) 4929–4941
polymer
www.elsevier.com/locate/polymer

Deformation mechanisms in rubber toughened semicrystalline polyethylene terephthalate

Wendy Loyens, Gabriël Groeninckx*

Department of Chemistry, Laboratory of Macromolecular Structural Chemistry, Katholieke Universiteit Leuven (KULeuven), Celestijnenlaan 200F, B-3001 Heverlee, Belgium

Received 28 August 2002; received in revised form 24 March 2003; accepted 30 May 2003

Abstract

The deformation mechanisms of rubber toughened polyethylene terephthalate (PET) are studied with fractography of impact fractured samples and tensile dilatometry. The dispersed phase consists of a mixture of an ethylene-*co*-propylene rubber (EPR) and a compatibilising agent (E-GMA8: copolymer of ethylene and 8 wt% of glycidyl methacrylate). It is found that the ductile fracture behaviour, above the brittle–ductile transition temperature (T_{bd}), consists of a high degree of rubber cavitation and extensive matrix shear yielding, both in the fracture plane and the stress whitened zone surrounding the crack. A steep increase in the volume strain upon tensile loading confirms the presence of the rubber voiding mechanism in the PET/(EPR/E-GMA8) blend system. It is seen that the stress whitened zone below the impact fracture surface consists of different zones, depending on the test temperature. Below T_{bd}, a layer of a highly deformed structure is followed by a cavitation layer containing only a limited number of cavitaties. Increasing the temperature, causes the deformation layer to be replaced by a zone lacking structure. It is believed that part of the fracture energy has been dissipated in the form of heat inducing a relaxation in the structure. Dynamical mechanical analysis under superimposed axial stresses reveals that the dispersed rubber particles internally cavitate in the presence of volume strain. At increased volume strains, the biaxial stress state in the cavitated particle is disturbed, resulting in the rupture of the rubber chains closest to the void by a tearing mechanism; revealing that the rubber particle is damaged upon cavitation.

Keywords: Rubber toughening; Deformation mechanism; Semicrystalline polyethylene terephthalate

1. Introduction

Rubber modification provides an effective method to improve the impact behaviour of notch sensitive semicrystalline polyethylene terephthalate (PET) [1–4]. The main role of the dispersed rubber particles is to induce an overall deformation mechanism, rather than a localised one. When toughening notch sensitive materials, the dispersed rubber particles are likely to cavitate and/or debond upon the application of a load. The voiding of the rubber phase leads to a relief of the triaxial stress state ahead of the notch or crack, thus creating a stress state beneficial for the initiation of multiple matrix shear yielding [3,5,6]. In recent years, several models have been developed which quantitatively describe the cavitational process. The models developed by Dompas and Groeninckx [7], and by Lazzeri and Bucknall [8,9] are based on an analogous principle. Void formation is stated to occur when the released internally stored stress build-up (volumetric strain energy) is greater than the energy required for the creation and expansion of the surface area of the void. The energy balance model of Lazzeri and Bucknall also stipulates that the energy released additionally needs to cover the energy required for the stretching of the surrounding rubber, adding an extra term to the equation. The volume strain energy present in the rubber particles can originate from two sources: mechanical loading and/or differential thermal contraction [10,11]. Fig. 1 illustrates the different steps involved during the event of rubber cavitation.

The deformation behaviour of rubber toughened thermoplastics is commonly investigated using tensile dilatometric [12–14], light scattering [10,15] or X-ray scattering [16] measurements. They are most often performed in real-time during uniaxial tensile deformation. In addition, the study of the fracture zone (stress whitened area) after loading using

* Corresponding author. Tel.: +32-16-327440; fax: +32-16-327990.
E-mail address: gabriel.groeninckx@chem.kuleuven.ac.be (G. Groeninckx).

0032-3861/03/$ - see front matter © 2003 Elsevier Science Ltd. All rights reserved.
doi:10.1016/S0032-3861(03)00478-6

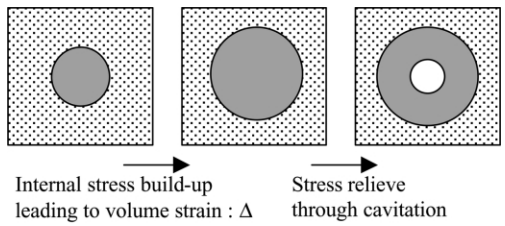

Fig. 1. Schematic presentation of the steps involved in rubber cavitation.

microscopy provides a direct view of the deformation mode. All these techniques provide information on large scale deformations, meaning that the rubber cavities have expanded from their initial small dimensions (< 10 nm) often in combination with matrix shear yielding.

To understand the cavitation process within the dispersed rubber particles, it is necessary to distinguish between the process of yielding and that of cavitation itself. Recently, Bucknall et al. [11,17] have developed a dynamic mechanical thermal spectroscopic technique (DMTS) that allows investigating cavitation as a separate process during the early stages of deformation in the absence of shear yielding. The technique is based on the principle that in the absence of internal voids, the density of the rubber phase in toughened thermoplastics will change upon the application of different axial stresses [18]. The T_g of the rubber phase will shift since its free volume is altered due to the imposed stresses. The application of an axial compression stress will increase the rubber density, and consequently shifts the rubber T_g to a higher temperature. In contrast, a shift of the T_g towards a lower temperature is expected upon the application of an axial tensile stress. The response to the application of tensile stresses can be very different, depending on the characteristics of the thermoplastic matrix/elastomer system [11,17]. The rubber T_g of high impact polystyrene (HIPS) [17] remained constant and thus unaffected by the application of a large range of axial tensile stresses. This provided a clear indication of the occurrence of a voiding mechanism in the rubber phase, resulting from either cavitation in the particles or debonding at the particle-matrix interface.

The present article is concerned with the study of the deformation mechanism present in rubber toughened semicrystalline PET. Previous work has revealed that the dispersion of a preblend of an ethylene-*co*-propylene rubber (EPR) and a copolymer of ethylene and 8 wt% of glycidyl methacrylate (E-GMA8) provides a very effective toughening route for semicrystalline PET [19]. Microscopical investigations of the fracture zone of the notched Izod impact fractured samples have been performed in order to clarify the deformation mechanism occurring upon loading. The influence of the sample composition, the morphological characteristics and the test temperature is examined. Additionally, tensile dilatometric measurements will be used to explore the presence of a voiding mechanism and matrix shear yielding during tensile loading. The onset of rubber cavitation is investigated by the earlier described dynamical mechanical testing technique. A wide range of both compression and tensile axial stresses is imposed on a highly ductile rubber toughened PET blend.

2. Experimental

2.1. Materials

The PET compound used was a grade from Shell Chemical ($Mn = 29,500$ g/mol and $\rho = 1.40$ g/cm^3) with trade name Caripak G82. The basic, non-reactive elastomer, EPR, with trade name Vistalon 805 (E/P ratio = 78/22, $\rho = 0.86$ g/cm^3) was kindly supplied by Exxon Chemical. The ethylene–glycidyl methacrylate copolymer, E-GMA8, (8 wt% GMA, MFI (190 °C, 2.16 kg) = 5 g/10 min) was supplied by Elf Atochem with trade name Lotader AX 8440.

2.2. Blend preparation and compounding

Before blending with PET, EPR and E-GMA8 were preblended at different ratios. The preblending was done on a Haake Rheocord 9000 batch mixer using a small mixing chamber of 69 cc at a temperature of 180 °C and a screw speed of 50 rpm during 5 min. The compounding of the actual rubber toughened blends was performed on the batch mixer using a mixing chamber of 300 cc at a temperature of 280 °C and a screw speed of 50 rpm during a total mixing time of 10 min. The compositions of the ternary PET/(elastomer/compatibiliser) blends are based on a constant weight concentration of the dispersed phase but with a changing ratio (EPR/E-GMA8) of the two dispersed phase components. After mixing, the blends were compression moulded into plaques. After an initial melting step at 280 °C, the mould was transferred directly into a second press held at a temperature of 180 °C for 5 min. After removal, the plaques were left to cool to room temperature. This procedure was applied carefully in order to control the overall crystallisation conditions.

2.3. Notched Izod impact testing and dynamic mechanical testing (DMTS)

Notched Izod impact tests were performed according to ISO-180 on a Zwick 5110 apparatus on samples machine-cut from the compression moulded plaques. The notch was milled in, having a depth of 2 mm, an angle of 45° and a notch radius of 0.25 mm. Prior to testing, the samples were dried overnight and subsequently kept at room temperature in an exiccator. At each temperature, at least five samples were tested and the results averaged.

The dynamic mechanical measurements were carried out on an Eplexor dynamic mechanical thermal spectrometer (DMTS) from Gabo Qualimeter. This instrument can apply static loads up to 1500N, either in tension or in compression,

while simultaneously measuring the dynamic mechanical thermal properties at small stress amplitudes. Rectangular bars ($4 \times 4 \times 10\ mm^3$) were milled from the compression moulded plaques for the axial compression tests. Dumb-bell shaped samples (gauge section: $4 \times 4 \times 20\ mm^3$) were milled for the axial tensile tests. The milled surfaces were polished with fine emery paper to prevent premature fracture in tension. The dynamic mechanical measurements were performed over a temperature range going from −80 to +20 °C at a heating rate of 2 °C/min and a frequency of 10 Hz; the dynamic strain was around 0.1–0.2%.

The respective dynamic and static stresses were applied in a direction parallel to the length of the specimen. The applied static stress ranged from −30 MPa (compression) to +25 MPa (tension) and was first applied to the specimen at room temperature. This imposed axial stress was kept constant during the subsequent dynamic mechanical measurements. For each stress level at least three samples in compression and four samples in tension were examined.

2.4. Microscopical SEM and TEM fractography

The fractographic study was performed on samples fractured by notched Izod impact testing at various test temperatures. Fig. 2 presents a scheme of the examined fracture planes. The fracture surface (*XY* plane), resulting from the separation of the sample halves, was investigated with scanning electron microscopy (SEM) after gold sputtering, without further alteration of the surface. The samples taken perpendicular to the fracture plane (*YZ* plane) were smoothened on a Leica Ultracut UCT microtome at −100 °C. Of each specimen, two SEM samples were prepared. One was etched in *m*-xylene at 105 °C to remove the minor phase while the other sample was only smoothened; no further etching was applied.

Transmission electron microscopy (TEM) was performed using a Philips CM 10 transmission electron microscope on samples taken in the *YZ* plane at two different sites. The first site was located as close as practically possible to the fracture surface. The second site was located at a distance of about 1 mm from the fracture surface. Slices with a thickness of 100 nm were cut on the Leica cryo-microtome at a temperature of −100 °C using a

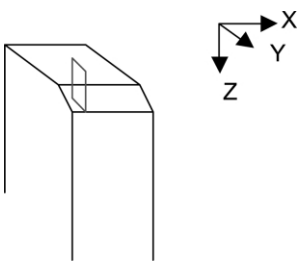

Fig. 2. Schematic presentation of the different sample planes in a fractured notched Izod impact sample; the outlined area (grey) refers to the sample plane in the *YZ* direction.

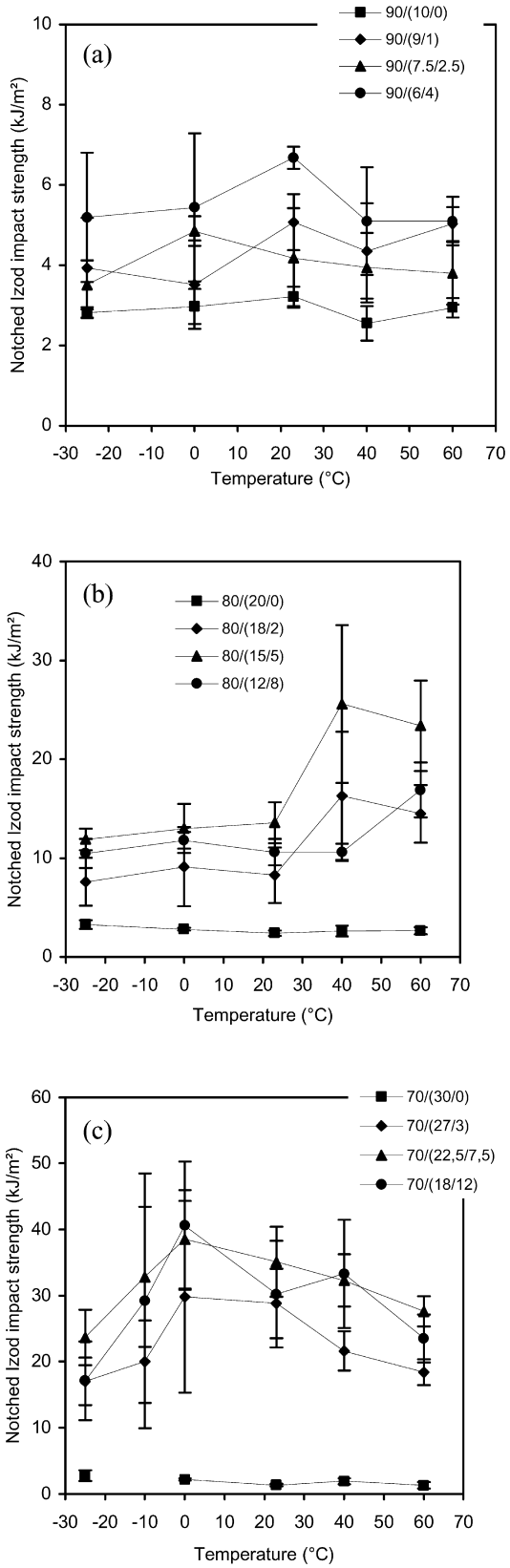

Fig. 3. Notched Izod impact strength as a function of the temperature for the PET/(EPR/E-GMA8) blends having the following dispersed phase compositions: (a) 90/(*x*/*y*); (b) 80/(*x*/*y*) and (c) 70/(*x*/*y*).

Table 1
Weight average particle diameter (D_w), interparticle distance (ID) and brittle–ductile transition temperature (T_{bd}) of the PET/(EPR/E-GMA8) blends as a function of the dispersed phase concentration and composition

Weight fraction of E-GMA8 in the dispersed phase (−)	D_w (μm)	ID (μm)	T_{bd} (°C)
10 wt%			
0	2.92 ± 0.18	1.49	80
0.1	0.60 ± 0.07	0.31	80
0.25	0.67 ± 0.06	0.34	80
0.4	0.80 ± 0.02	0.40	80
20 wt%			
0	6.45 ± 0.61	1.45	80
0.1	0.55 ± 0.08	0.12	40
0.25	0.61 ± 0.09	0.14	31
0.4	0.43 ± 0.08	0.10	50
30 wt%			
0	9.5 ± 0.9	0.56	80
0.1	0.65 ± 0.09	0.058	−5
0.25	0.41 ± 0.03	0.036	−15
0.4	0.53 ± 0.04	0.047	−10

diamond knife. OsO_4 was used to stain the semicrystalline PET matrix.

2.5. Tensile dilatometry

The tensile dilatometric measurements were performed on dumb-bell shaped specimens prepared according to ISO 527 (gauge dimensions: $80 \times 10 \times 4$ mm^3) from compression moulded plaques. The milled surfaces were polished with fine emery paper to prevent surface deficiencies. The uniaxial tensile testing was performed on an Instron 4505 at a test speed of 1 mm/min. Two extensometers were used to measure the longitudinal and the transverse strain. The thickness strain was assumed to be identical to the transverse strain. The volume strain $\Delta V/V_0$ is calculated according to the following formula [6]:

$$\frac{\Delta V}{V_0} = (1 + \varepsilon_l)(1 + \varepsilon_t)^2 - 1 \quad (1)$$

where ΔV is the volume change, V_0 is the original volume and ε_l and ε_t are the longitudinal and the transverse nominal strains, respectively.

3. Results and discussion

3.1. Notched Izod impact behaviour of rubber toughened PET as a function of the temperature

The notched Izod impact strengths of the PET/(EPR/E-GMA8) blends as a function of the temperature is presented in Fig. 3(a)–(c). A more extensive discussion is provided in our previous publication [4]. It can be seen that the dispersed phase concentration and composition have a strong effect on the impact behaviour of rubber toughened PET. Within the investigated temperature range, the 90/(*x*/*y*) blends fail in a brittle manner displaying a low fracture energy. It can be anticipated that their actual brittle–ductile transition temperature (T_{bd}) will be situated in the vicinity of the glass-transition temperature of the PET matrix (± 80 °C). The T_{bd}'s of the 80/(*x*/*y*) blends are found to be located at elevated temperatures (40–50 °C). At room temperature, only the 70/(*x*/*y*) blends fail according to a ductile fracture mode, revealing a high fracture toughness and extensive stress whitening. Their brittle–ductile transition temperatures are located well below room temperature.

The T_{bd} of the ternary PET/(EPR/E-GMA8) blend clearly decreases with increasing dispersed phase concentration (Table 1). Accordingly, the necessity of a minimum dispersed phase concentration becomes obvious in order to attain room temperature tough materials. The presence of the compatibilising agent, E-GMA8, is a prerequisite for obtaining impact tough materials. As reported previously [4], the marked differences between the various blend compositions can be attributed to their respective differences in morphological characteristics. As can be seen from Table 1, there exists a distinctly strong correlation between the T_{bd} and the interparticle distance (ID) as the T_{bd} is found to decrease with a decreasing ID. The interparticle distance is defined as the distance between two adjacent rubber particles. The 70/(*x*/*y*) blends have the smallest interparticle distances and accordingly display the lowest brittle–ductile transition temperatures, resulting in the observed good low temperature toughness. In order to obtain room temperature tough PET, a critical interparticle distance of 0.1 μm needs to be reached [4]. From Table 1 it becomes clear that only reactively compatibilised 30 wt% rubber blends have interparticle distances below this value and thus display a high fracture toughness at room temperature.

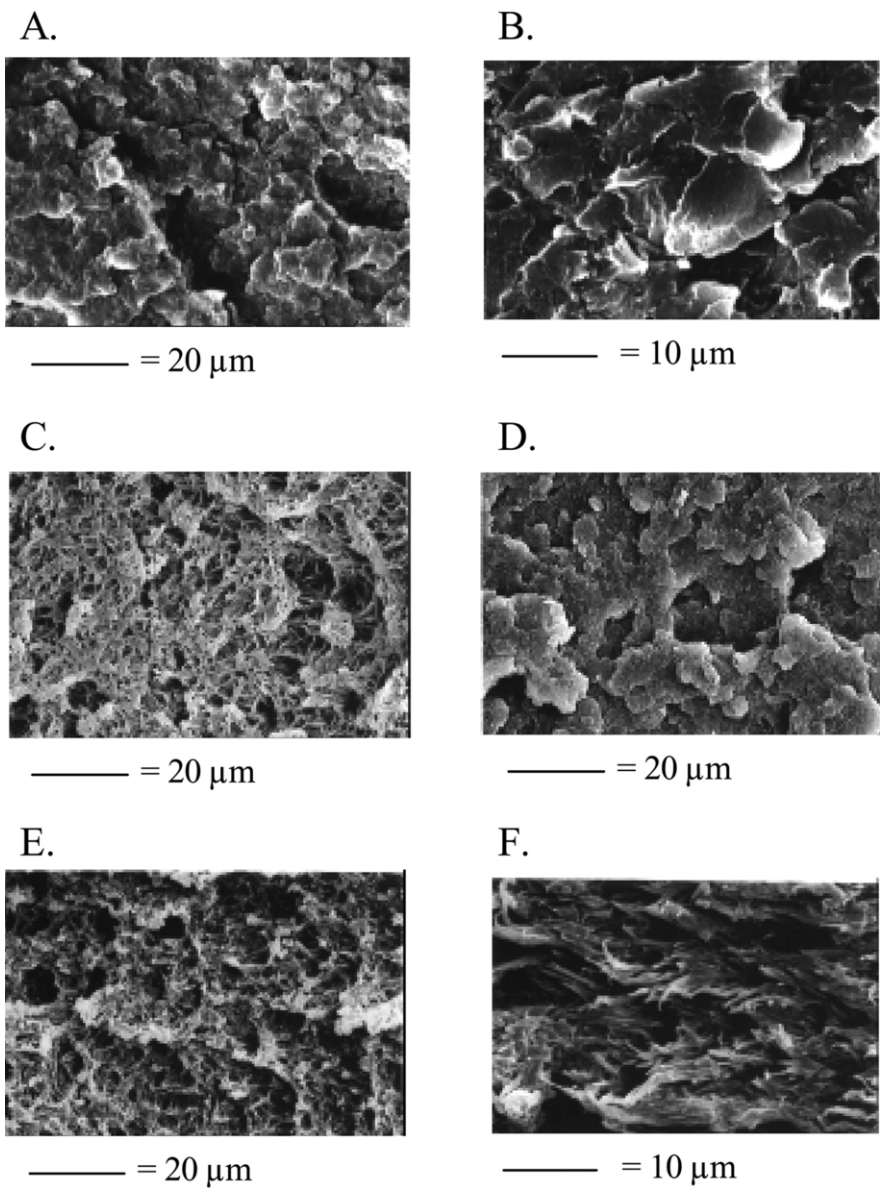

Fig. 4. SEM micrographs of the fracture surface in the *XY* plane (the fracture runs from right to left). The left column represents the structure directly behind the notch whereas the right column presents the structure at 300 μm from the notch for the following compositions: [A,B] 90/(7.5/2.5); [C,D] 80/(15/5) and [E,F] 70/(22.5/7.5).

3.2. Fractography

3.2.1. Impact fracture zone structure of brittle and ductile fractures at room temperature

The structure of the fracture surface and the stress whitened zone provides direct information with regard to the occurring deformation mechanism and the stability of the propagating crack upon loading. The observation of stress whitened zones on impact fractured PET/(EPR/E-GMA8) blends is not obvious. The samples already have a distinct white colour on account of their semicrystalline nature and the difference in refractive index between the matrix and the dispersed phase particles. Only intense stress whitening could be observed as a circular zone surrounding the crack.

Fig. 4 presents the fracture surfaces (*XY* plane) of the PET/(EPR/E-GMA8) blends for different dispersed phase concentrations, having an E-GMA8 content of 25 wt% in the dispersed phase composition. The SEM micrographs are taken directly behind the notch and at a distance of ± 300 μm. The low impact strengths (< 10 kJ/m^2) of the 90/(*x*/*y*) blends are clearly reflected by their fracture surfaces. They reveal the typical characteristics of a brittle failure; a relatively flat, smooth surface without any sign of deformation. Upon impact, the two sample halves are completely separated at a very high fracture speed, typical of an unstable fracture [20]. There exists a relatively good

adhesion between the PET matrix and the dispersed phase as no separate particles can be observed. The 80/(*x*/*y*) blends also display a brittle fracture mode at room temperature, but their fracture surfaces have a slightly different structure. A small hemispherical zone is located directly behind the notch, consisting of stretched matrix material and the presence of voids due to cavitation/debonding of the rubber particles (Fig. 4(C)). Matrix shear yielding has clearly occurred and deformed the rubber particles. The fracture is thus initiated in a stable, ductile manner. The propagating crack, however, quickly becomes unstable due to an insufficient dissipation of energy, resulting in a brittle fracture (Fig. 4(D)).

This is confirmed by the SEM micrographs taken in the *YZ* plane, perpendicular to the fracture surface (Fig. 5). The small, spherical holes result from voiding of the rubber particles since the samples were not etched and no matrix crazing was observed. This voiding zone can be referred to as a 'cavitation layer' [10,21]. It starts directly below the fracture surface with no evidence of matrix yielding. The number of cavitated particles is rather limited. The propagating crack becomes unstable due to the low amount of dissipated energy. From Table 1 and our previous publication [19], the interparticle distances of the 80/(*x*/*y*) compositions were found to be too high in order to reach the critical interparticle distance of 0.1 μm.

The ductility of the 70/(*x*/*y*) blends is clearly visualised by their fracture surfaces (Fig. 4(E) and (F)). The matrix has yielded significantly and has deformed the dispersed phase particles (original size = ±0.4 μm). Rubber cavitation is clearly visible. A macroscopical sized stress whitened zone, typical for a ductile fracture, could be observed to surround the crack [20,22]. The structure near the end of the fracture surface (Fig. 4(F)) consists of strongly deformed, fibrillated material. The corresponding amount of plastic deformation is high and effectively dissipates the fracture energy, resulting in the observed highly improved impact strengths at room temperature (Fig. 3(c)).

The structure of the stress whitened zone (*YZ* plane) provides a further insight of the occurring deformation mechanism (Fig. 6) [10,23]. A cavitation layer containing a high number of cavities of various sizes can be clearly observed. The detailed micrograph of Fig. 6 illustrates the high degree of cavitation. However, this cavitation layer does not start directly at the fracture surface. A second zone containing almost no cavities and lacking any structure is located directly below the fracture plane. This becomes more clear from Fig. 7 presenting the fracture zone structure in the *YZ* plane, directly below the fracture plane, of an etched sample. The small zone lacking any structure can be clearly observed.

The fractographic study of rubber toughened polyamides (PA) and polypropylene (PP) has revealed a similar non-cavitated zone, determined a 'relaxation layer' [10,23]. The lack of structure suggests that the initially present deformation has relaxed. This can only occur when the material is elastic enough to undergo a relaxation process. It is believed that part of the fracture energy has dissipated in the form of heat during the high speed impact test [10,23,24]. The corresponding temperature rise around the propagating crack can explain the relaxation of the structure. The formed layer also leads to a blunting and stabilisation effect of the propagating crack, resulting in an additional increase in the impact strength (Fig. 3(c)). The relaxation layer of the rubber toughened PET systems has an average length of ±15 μm.

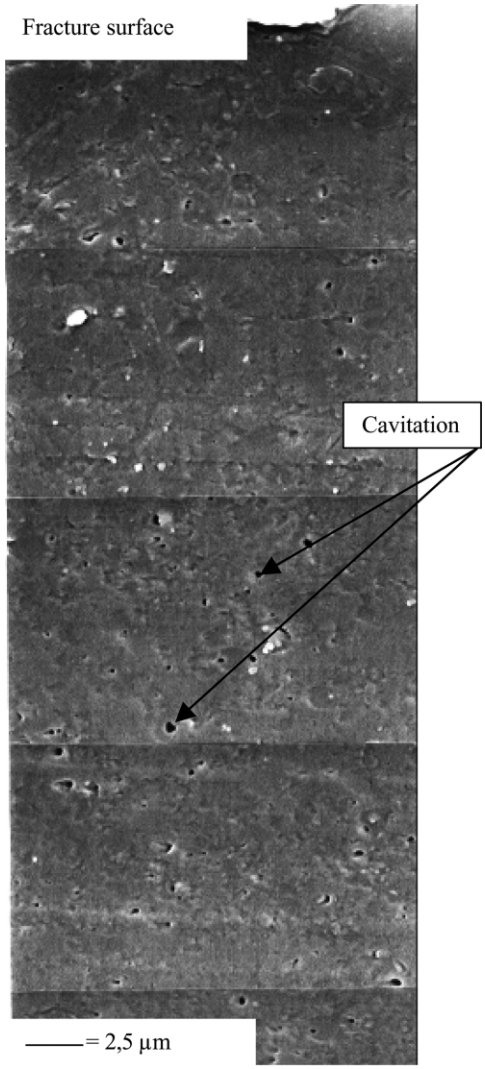

Fig. 5. Fracture zone in the *YZ* plane of the PET/(EPR/E-GMA8) 80/(15/5) blend (smoothened and non-etched), fractured at room temperature. The fracture plane is located at the top and the fracture propagates from right to left.

3.2.2. Impact fracture zone structure at various temperatures

The deformation and fracture behaviour of rubber toughened PET is highly influenced by the temperature (Fig. 3(a)–(c) and Table 1). The fracture zone accordingly

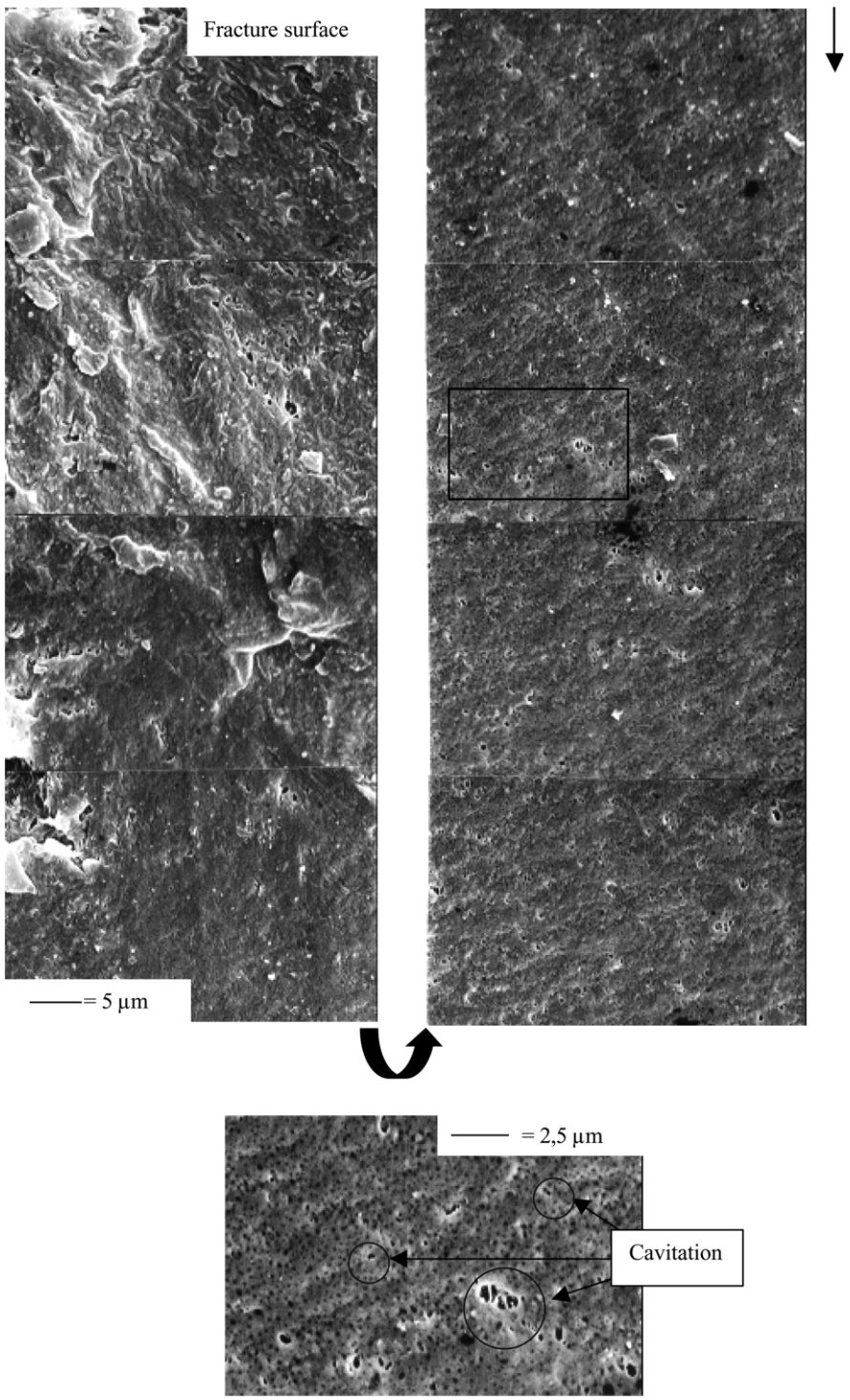

Fig. 6. Fracture zone in the *YZ* plane (smoothened and non-etched) of the PET/(EPR/E-GMA8) 70/(22.5/7.5) blend, fractured at room temperature. The fracture plane is located at the top and the fracture propagates from the right to the left. The detailed micrograph is taken at the indicated position.

reflects the influence of the temperature on the fracture behaviour. Fig. 8 provides an overview of SEM micrographs of the impact fracture surfaces (*XY* plane) of rubber toughened PET at different temperatures. At a temperature of −25 °C (Fig. 8(A) and (B)), the blends are fractured well below their respective T_{bd}. A limited amount of plastic deformation is visible, directly behind the notch. The crack, however, propagates in an unstable manner, resulting in an overall brittle fracture mode. Rubber toughened PET blends fractured at temperatures above their T_{bd} (Fig. 4(E) and (F) (20 °C) and Fig. 8(C) and (D) (60 °C)), clearly reveal extensive matrix shear yielding and rubber cavitation, over the entire fracture surface, clearly illustrating the

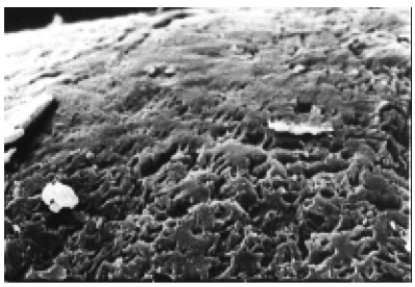

Fig. 7. SEM micrograph of the fracture zone in the *YZ* plane directly below the fracture plane (smoothened and etched) of the PET/(EPR/E-GMA8) 70/(22.5/7.5) blend fractured at room temperature.

ductile fracture mode. No significant structural differences could be observed between test temperatures above T_{bd}.

The structure of the stress whitened zone (*YZ* plane) as a function of the test temperature reveals an interesting evolution. At a temperature of −25 and 0 °C (Fig. 9(A) and (B), scheme d), voiding starts directly below the fracture plane. Up to a depth of ±30 μm, the cavities are seen to have an elongated and oriented shape, most likely caused by matrix shear yielding (deformation layer) [10,23,24]. It is followed by a second layer containing small, non-deformed spherical cavities. Fig. 10(A) further illustrates the fracture zone at 0 °C when the minor phase has been etched away, clearly revealing a deformed structure.

With increasing impact test temperature the deformed structure can apparently relax, as illustrated by the etched and non-etched SEM micrographs in Figs. 6, 7, 9(C) and 10(B). The structure of the stress whitened zone directly under the fracture surface no longer contains deformed cavities and displays a lack of structure. This is in good agreement with the earlier discussed observations of the layered structure of the fracture zone at room temperature (Fig. 6). The average length of the relaxation layer remains fairly constant, despite the changing temperature. The relaxation layer is followed by the cavitation layer. Fig. 9(D) and (E) provides a schematic presentation of the observed different deformation structures.

The majority of cavities have a nanometer size, although several voids have grown out to bigger dimensions (Figs. 6 and 9(C)). The cavitational models predict that larger rubber particles cavitate in the early stages of deformation, giving rise to larger cavities [7,8]. With increasing test temperature, the cavity size increases on account of the decreased elastic modulus of the rubber phase which facilitates the cavitation process.

The TEM pictures presented in Fig. 11 provide a more detailed view of the fracture structure. The contrast of the pictures is not optimal as PET was very sensitive to the

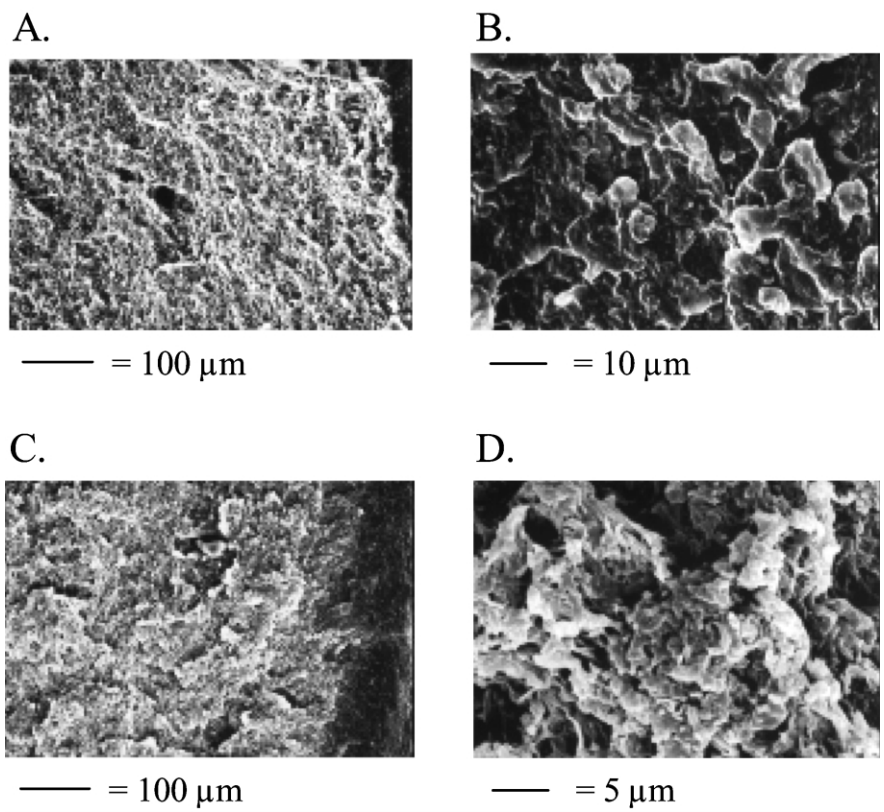

Fig. 8. SEM micrographs of the fracture surfaces in the *XY* plane of the PET/(EPR/E-GMA8) 70/(22.5/7.5) blend fractured at various test temperatures: [A,B] −25 °C; [C,D] 60 °C. The left column presents the structure directly behind the notch whereas the right column presents the structure at ±500 μm.

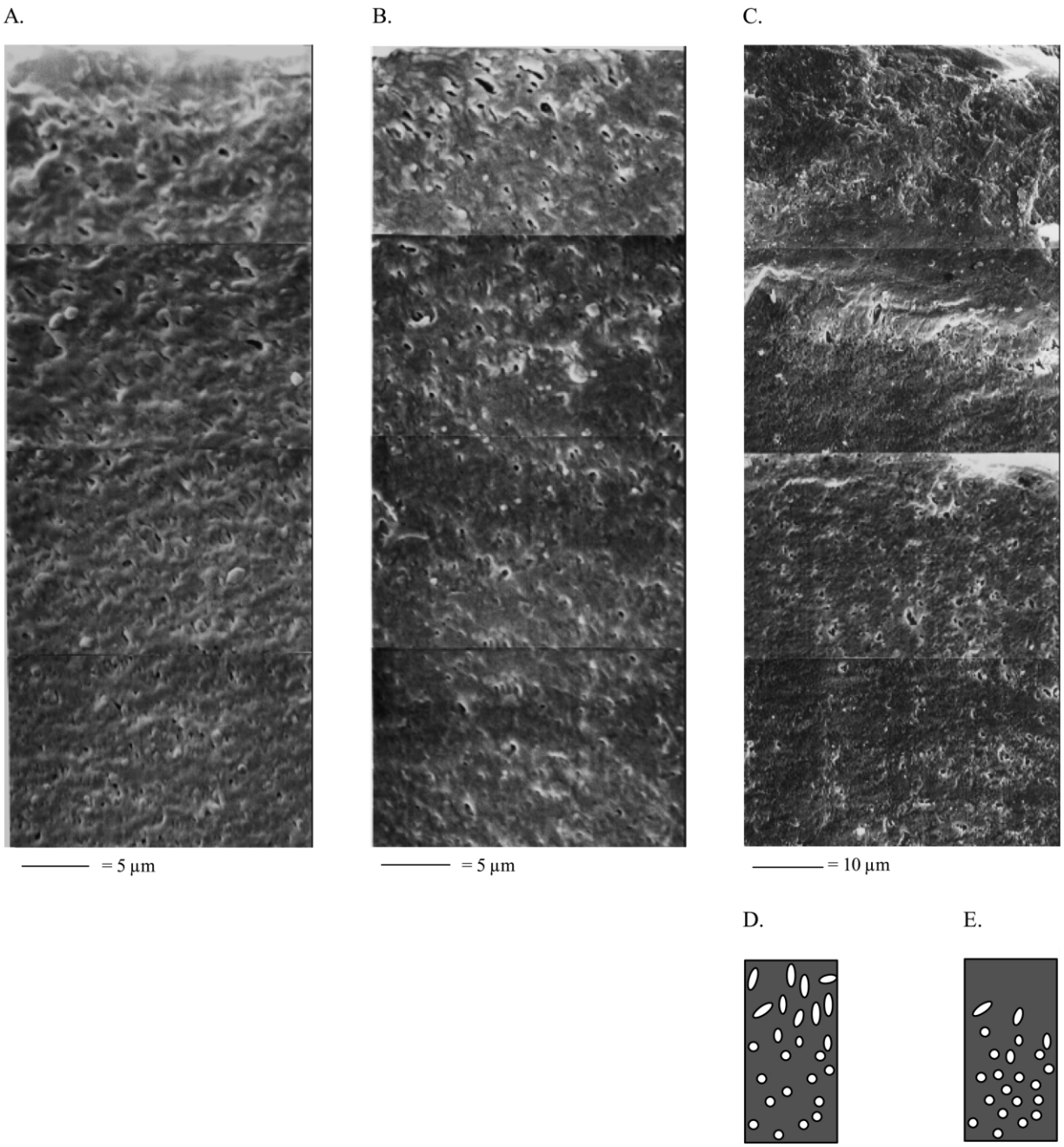

Fig. 9. SEM micrographs of the fracture zone (smoothened and non-etched) in the *YZ* plane of PET/(EPR/E-GMA8) 70/(22.5/7.5) blend, fractured at [A] −25 °C; [B] 0 °C; [C] 60 °C. The crack runs from the right to the left. Schematic presentations of the deformation structure in the *YZ* fracture plane below T_{bd} [D] and above T_{bd} [E].

electron beam. Fig. 11(A) presents the blend phase morphology at a distance of ±3 mm from the fracture surface in the *YZ* plane. The matrix and the dispersed phase particles can be clearly observed. The two dispersed phase components (EPR and E-GMA8) cannot be distinguished from each other. Due to the large distance from the fracture surface, no cavities could be detected. Fig. 11(B) is taken near the fracture plane of a sample fractured at −25 °C, showing non-deformed, cavitated particles. This is in good agreement with the structure of the stress whitened zone (*YZ*) observed with SEM. No debonding or matrix yielding could be observed.

The samples fractured at room temperature and 60 °C reveal a clearly different structure (Fig. 11(C) and (D)). The rubber particles have been highly deformed due to extensive matrix shear yielding, possibly in combination with the earlier discussed temperature rise near the fracture surface during crack propagation. A few cavities within the particles can be observed.

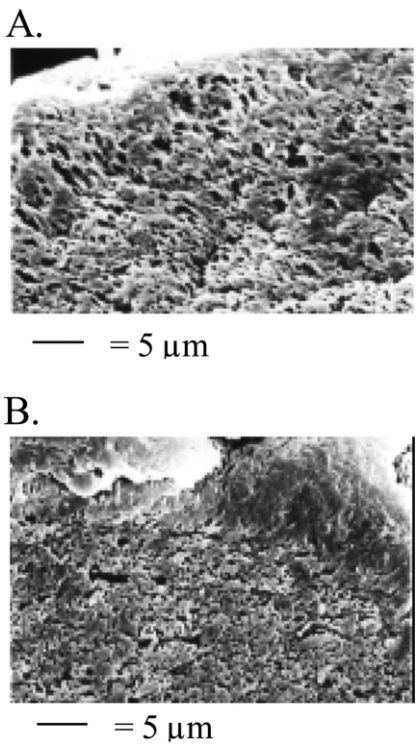

Fig. 10. Smoothened and etched fracture zone in the *YZ* plane directly below the fracture plane of the PET/(EPR/E-GMA8) 70/(22.5/7.5) blend at the following impact test temperatures: [A] 0 °C; [B] 60 °C.

3.3. Deformation behaviour of rubber toughened PET during uniaxial tensile dilatometry

Deformation processes involving the formation of voids like cavitation, debonding and crazing are dilatational processes, whereas shear yielding proceeds at a constant volume. The course of the volume strain during uniaxial tensile testing provides information about the mode of deformation occurring in rubber toughened thermoplastics upon loading.

Fig. 12 presents the simultaneously measured tensile and dilatometric data of the PET/(EPR/E-GMA8) 70/(18/12) blend. The stress and the volume strain are presented as a function of the measured longitudinal strain. The yield point is located at a longitudinal strain of $\pm 3.8\%$. Visual inspection of the samples revealed a uniform distribution of the deformation over the entire gauge section. As a consequence, the samples exhibited no observable neck formation upon yielding. The appearance of stress whitening during tensile testing was difficult to detect due to the white colour of the samples.

The volume strain is calculated according to Eq. (1) based on the experimental longitudinal and transverse strains. Since the samples did not exhibit neck formation, the volume strain results remain valid after yielding. The initial linear increase in the volume strain ($\varepsilon_l \cong 0$–3.3%) can be mainly attributed to homogeneous elastic deformation with a constant lateral contraction ratio (Poisson effect). After this initial response, a steep increase in the slope, and thus of the volume strain can be observed. This is caused by the occurrence of a voiding process [25–27]. It has been reported in literature that the type of microvoiding mechanism is not altered from low to high strain rates [10,23,26]. It can therefore, be assumed that the deformation mechanism observed during impact testing remains valid under the conditions present during uniaxial tensile testing. The obvious increase in the volume strain can therefore, be assigned to a considerable amount of rubber cavitation. The high amount of volume strain originates from the high dispersed phase volumetric concentration of 40 vol%. The volume strain is known to increase with an increasing concentration of dispersed rubber particles, which during deformation results in a high amount of cavitation [13,25]. Rubber cavitation causes the reduction of the cross-section upon yielding to occur uniformly throughout the gauge section, inhibiting macroscopic necking. The onset of cavitation is situated in the vicinity of the yield point [12,13,15,25].

3.4. Cavitational behaviour of rubber toughened PET under superimposed axial tensile and compression stresses

The cavitational behaviour of the dispersed phase in rubber toughened PET is explored for the PET/(EPR/E-GMA8) 70/(22.5/7.5) blend, displaying a ductile fracture behaviour at room temperature. Both dispersed phase components are not miscible and their respective glass-transition temperatures remain located at the position of the pure component, regardless of the blend composition (T_g of EPR $\cong -40$ °C and T_g of E-GMA8 $\cong -15$ °C) [28]. Since, cavitation is dominated by the rubbery dispersed phase component, the glass-transition of EPR will be regarded. Figs. 13 and 14 present the dynamic mechanical responses of EPR upon the application of static compression and tensile stresses, respectively. The dynamic mechanical tests were performed over a wide range of stresses, going from -30 up to $+25$ MPa. The $\tan\delta$ curves are relatively broad, all exhibiting a similar shape. The broadness originates from the copolymeric structure of EPR.

In Fig. 15 the experimentally established glass-transition temperatures of EPR are plotted as a function of the applied axial stress. The response upon the application of an axial compression stress (-5 to -30 MPa) reveals a very clear trend. The T_g of EPR linearly increases with increasing compression stress. Increasing the compression stress will increase the rubber density, and correspondingly decrease the free volume. This inevitably leads to an increase in the rubber T_g. If cavities are present, they will be closed by the compression.

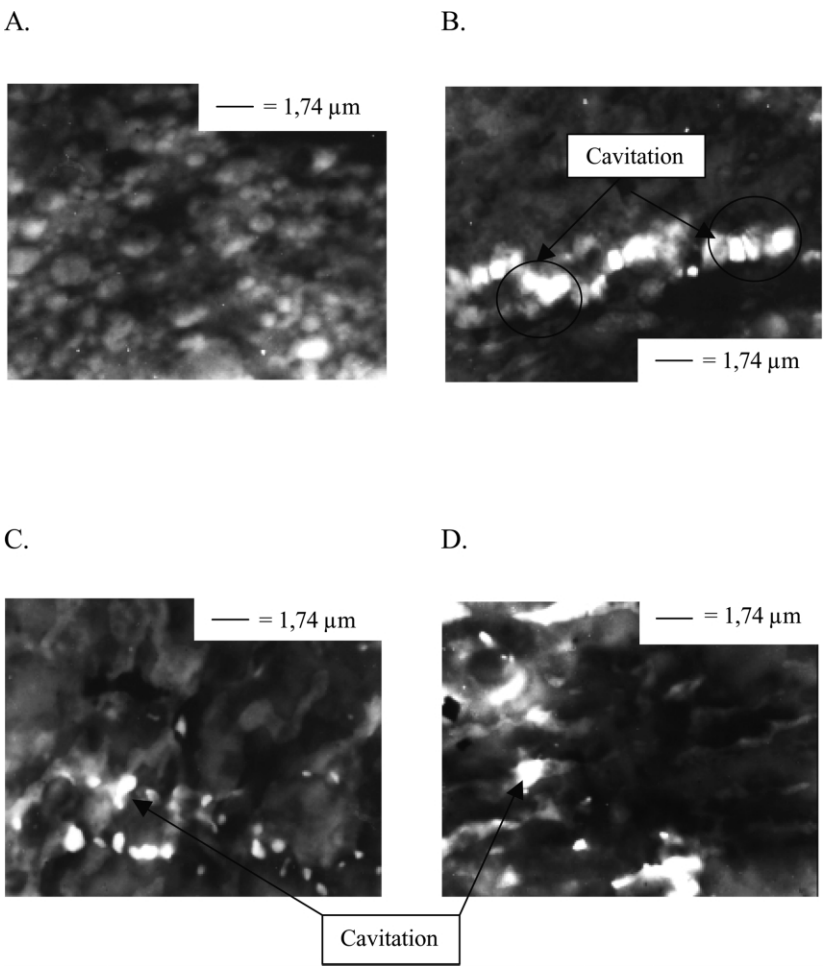

Fig. 11. TEM micrographs of the fracture zone of the PET/(EPR/E-GMA8) 70/(22.5/7.5) blend in the *YZ* plane: [A] at some distance from the fracture plane at −25 °C; directly below the fracture plane at various fracture test temperatures: [B] −25 °C [C] 23 °C and [D] 60 °C.

The tan δ response upon the application of an axial tensile stress appears less obvious. Up to +5 MPa, the T_g values are found to lie on the extrapolated curve of the compression data. Between +5 and +15 MPa, however, the T_g becomes largely independent of the applied axial tensile stress. The application of higher tensile stresses ($\geq$20 MPa) leads to an obvious increase in the tan δ peak temperatures.

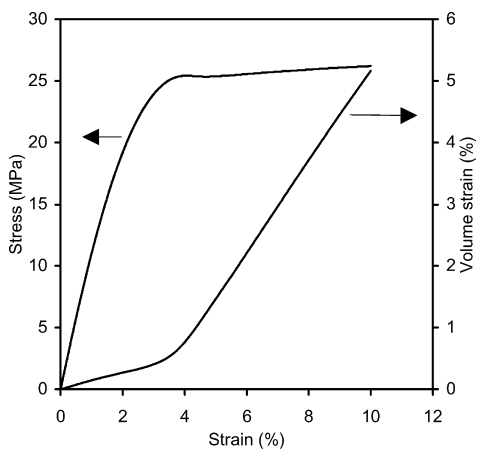

Fig. 12. Stress (—) and volume strain (–) as a function of the longitudinal strain for the PET/(EPR/E-GMA8) 70/(18/12) blend at room temperature during uniaxial tensile testing.

In order to understand the observed dynamic mechanical response of EPR upon the application of static tensile stresses, several considerations need to be taken into account. Fig. 16 is taken from Ref. [11] and provides a good overview of the various states possible after cavitation of the rubber phase. Position A represents the glass-transition temperature of so-called fully relaxed rubber particles. This state is reached when the particles have cavitated and the remaining stresses and strains have fallen to zero. The initially present volume strain (due to external loading and/or thermal contraction) becomes fully relieved, enabling the rubber phase to return to its equilibrium density and corresponding T_g [8,29]. It is also possible that the dispersed rubber particles display an incomplete or partial relaxation upon cavitation, resulting in T_g values located between point A and B (Fig. 16). A third possible state, concerns rubber particles which have not relaxed and remain subjected to an

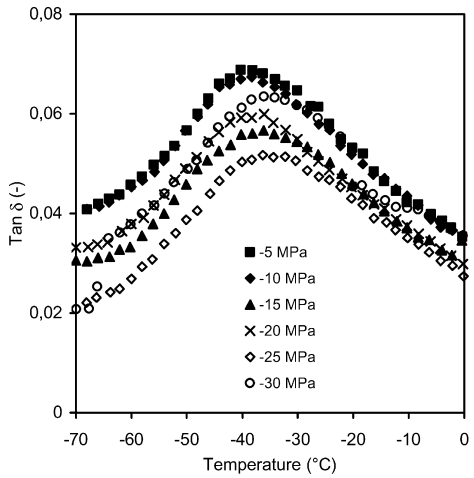

Fig. 13. Tan δ DMTA response of EPR upon the application of various axial compression stresses.

incompletely relieved volume strain, resulting in lower T_g values.

The observed independence of the T_g of EPR of the static axial tensile stress, between +5 and +15 MPa, has been reported before for HIPS and rubber toughened polymethyl methacrylate (PMMA) [11,17]. This independence provides a clear indication that failure has occurred in the rubber phase, in the form of rubber particle cavitation and/or debonding at the particle/matrix interface. The voiding mechanisms will render the rubber density independent of the applied stress. The glass-transition temperatures are situated in the lower temperature region, revealing that no relaxation has occurred in the rubber particles after cavitation.

Upon the application of higher tensile stresses ($\geq$20 MPa), the cavitated particles reveal a partial relaxation, resulting in increased glass-transition temperatures. Increasing the applied tensile stress causes a linear increase in the T_g of EPR. It is important to note that within a cavitated homogeneous rubber particle, the rubber becomes

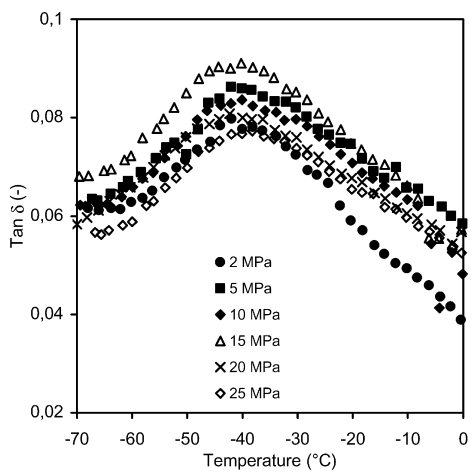

Fig. 14. Tan δ DMTA response of EPR upon the application of various axial tensile stresses.

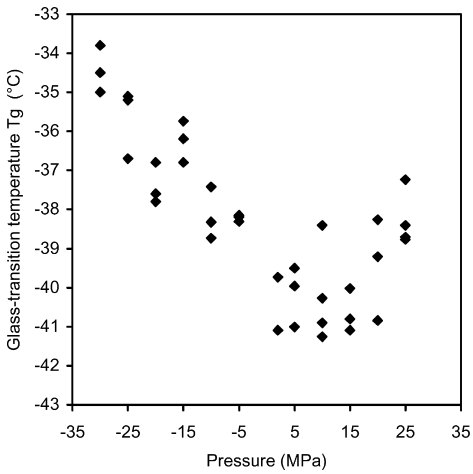

Fig. 15. Comprehensive graph presenting the glass-transition temperature of EPR as determined from the tan δ response upon the application of various uniaxial stresses.

subjected to a biaxial tension. This arises from the fact that the rubber chains can only stretch moderately at the matrix-particle interface, whereas the stretch ratio can theoretically reach infinity at the void surface. Consequently, a non-uniform stress distribution is present in the rubber particle after void formation that causes the particle to become less resistant against deformation. For a solid rubber particle, the present volume strain causes the cavity to grow, involving the rupture of the rubber chains closest to the void by a tearing mechanism. The chains of a crosslinked rubber are reported to fail at an extension ratio of 4 [29]. The increased glass-transition temperatures of EPR with increasing axial tensile stress can be attributed to the lower resistance of the cavity against the applied stress. The void formation and subsequent growth under the influence of higher applied stresses will result in an increased dissipation of the stored energy [8,30].

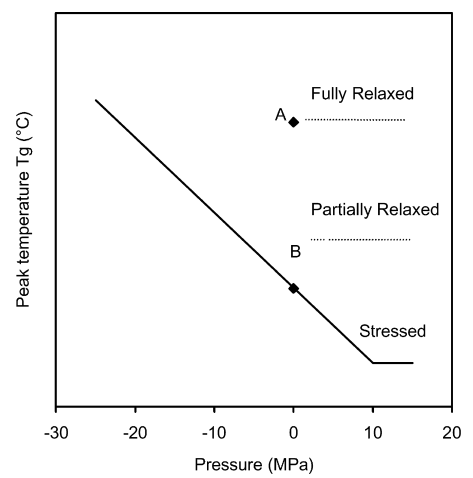

Fig. 16. Schematic diagram presenting the possible states of the rubber phase upon cavitation, reflected by the relative position of the glass-transition temperature.

4. Conclusions

A clarification of the deformation mechanisms occurring in rubber toughened PET upon loading has been provided. The transition from a brittle to a ductile fracture mode is accompanied by a distinct change of the fracture characteristics. The modified blends display a clear brittle fracture mode below the brittle–ductile transition temperature, characterised by a very limited amount of rubber cavitation.

Above T_{bd}, the rubber toughened semicrystalline PET systems display a distinctly ductile fracture behaviour. The deformation mechanism consists of a high degree of rubber cavitation and extensive matrix shear yielding, in the fracture plane and in the stress whitened zone surrounding the crack. A steep increase in the volume strain upon tensile loading confirmed the presence of the rubber voiding mechanism in the PET/(EPR/E-GMA8) blend system.

The stress whitened zone below the fracture surface of the rubber toughened PET system consists of several different zones, depending on the impact test temperature. Below T_{bd}, a small layer consisting of highly deformed and oriented particles is followed by a cavitation layer containing a limited number of cavitaties within the dispersed phase particles. As the temperature is increased, the deformation layer directly below the fracture surface is replaced by zone lacking structure. Part of the fracture energy is believed to have been dissipated in the form of heat. This results in a relaxation of the deformed structure and a stabilisation of the propagating crack by a blunting effect.

Dynamical mechanical analysis under superimposed axial stresses provided a useful tool for the study of the process of rubber cavitation. The dispersed rubber particles displayed an internal failure (cavitation) in the presence of volume strain that resulted from the external tensile stress and/or thermal contraction. At increased volume strains, the biaxial stress state in the cavitated particle is disturbed, involving the rupture of the rubber chains closest to the void by a tearing mechanism; revealing that the rubber particle is damaged upon cavitation.

Acknowledgements

The authors are indebted to the IWT-Belgium for a grant to one of them (W. Loyens) and the KULeuven Research Council for financial support of the laboratory (GOA blend project 98/06). They would also like to thank Prof. Clive Bucknall and Dr Rosi Rizzieri of the Cranfield University for the use of the GABO DMA and their expert guidance and discussions. The department of Material Science of KULeuven is thanked for their assistance with the tensile dilatometric measurements.

References

[1] Wu S. Polym Int 1992;29:229–47.
[2] Gaymans RJ. In: Paul DR, Bucknall CB, editors. Polymer blends: performance, vol. 2. New York: Wiley; 2000. Chapter 25.
[3] Hourston DJ, Lane S. In: Collyer AA, editor. Rubber toughened polymers. Cambridge: Chapman & Hall; 1994. Chapter 8.
[4] Loyens W, Groeninckx G. Polymer 2003;44(1):123–36.
[5] Kinloch AJ, Young RJ. In: Kinloch AJ, Young RJ, editors. Fracture behaviour of polymers. Essex: Applied Science Publishers; 1983.
[6] Bucknall CB. Toughened polymers. Essex: Applied Science Publishers; 1977.
[7] Dompas D, Groeninckx G. Polymer 1994;35(22):4743–9.
[8] Lazzeri A, Bucknall CB. J Mater Sci 1993;28:6799–808.
[9] Bucknall CB, Karpodinis A, Zhang XC. J Mater Sci 1994;29:3377–83.
[10] Dijkstra K. PhD Thesis. University of Twente, The Netherlands; 1993.
[11] Bucknall CB, Rizzieri R, Moore DR. Polymer 2000;41:4149–56.
[12] Okamoto M, Shinoda Y, Kojima T, Inoue T. Polymer 1993;34(23):4868–73.
[13] Borggreve RJM, Gaymans RJ, Eichenwald HM. Polymer 1989;30:78–83.
[14] Parker DS, Sue H-J, Huang J, Yee AF. Polymer 1990;31:2267–77.
[15] Dompas D, Groeninckx G, Isogawa M, Hasegawa T, Kadokura M. Polymer 1994;35(22):4750–9.
[16] Bubeck RA, Buckley DJ, Kramer EJ, Brown HR. J Mater Sci 1991;26:6249–59.
[17] Lin CS, Ayre DS, Bucknall CB. J Mater Sci Lett 1998;17:669–71.
[18] Morbitzer L, Kranz D, Humme G, Ott KH. J Appl Polym Sci 1976;20:2691–704.
[19] Loyens W, Groeninckx G. Polymer 2002;43(21):5679–91.
[20] Vu-Khanh T. Polymer 1988;29:1979–84.
[21] Van der Wal A, Verheul AJJ, Gaymans RJ. Polymer 1999;40:6057–65.
[22] Wu S. J Appl Polym Sci: Polym Phys Ed 1983;21:699–716.
[23] Van der Wal A, Gaymans RJ. Polymer 1999;40:6067–75.
[24] Muratoglu OK, Argon AS, Cohen RE, Weinberg M. Polymer 1995;36(5):921–30.
[25] Bucknall CB, Lazzeri A. J Mater Sci 2000;35:427–35.
[26] Dekkers MEJ, Hobbs SY, Watkins VH. J Mater Sci 1988;23:1225–30.
[27] Yee AF, Pearson RA. J Mater Sci 1986;21:2462–74.
[28] Loyens W, Groeninckx G. Macromol Chem Phys 2002;203(10/11):1702–15.
[29] Bucknall CB. In: Paul DR, Bucknall CB, editors. Polymer blends: performance, vol. 2. New York: Wiley; 2000. Chapter 22.
[30] Ayre DS, Bucknall CB. Polymer 1998;39(20):4785–91.